Cross- and Intra-image Prototypical Learning for Multi-label Disease Diagnosis and Interpretation

Chong Wang, *Member, IEEE*, Fengbei Liu, Yuanhong Chen, Helen Frazer, Gustavo Carneiro

arXiv:2411.04607v2 [cs.CV] 4 Apr 2025

***Abstract*—Recent advances in prototypical learning have shown remarkable potential to provide useful decision interpretations associating activation maps and predictions with class-specific training prototypes. Such prototypical learning has been well-studied for various single-label diseases, but for quite relevant and more challenging multi-label diagnosis, where multiple diseases are often concurrent within an image, existing prototypical learning models struggle to obtain meaningful activation maps and effective class prototypes due to the entanglement of the multiple diseases. In this paper, we present a novel Cross- and Intra-image Prototypical Learning (CIPL) framework, for accurate multi-label disease diagnosis and interpretation from medical images. CIPL takes advantage of common cross-image semantics to disentangle the multiple diseases when learning the prototypes, allowing a comprehensive understanding of complicated pathological lesions. Furthermore, we propose a new two-level alignment-based regularisation strategy that effectively leverages consistent intra-image information to enhance interpretation robustness and predictive performance. Extensive experiments show that our CIPL attains the state-of-the-art (SOTA) classification accuracy in two public multi-label benchmarks of disease diagnosis: thoracic radiography and fundus images. Quantitative interpretability results show that CIPL also has superiority in weakly-supervised thoracic disease localisation over other leading saliency- and prototype-based explanation methods.**

***Index Terms*—Multi-label Classification, Disease Diagnosis, Disease Interpretation, Prototypical Learning, Prototypes, Co-attention, Chest X-rays, Fundus Images.**

I. Introduction

THE last decade has witnessed the success of deep learning [1], [2], e.g., deep neural networks (DNNs), in supporting disease diagnosis and treatment in healthcare, including disease classification [3]–[6], lesion detection [7], [8], and organ segmentation [9]–[11]. Typically, DNNs require intricate network architectures, high-dimensional feature representations, and a massive number of trainable network parameters, posing significant challenges in interpreting the internal mechanisms of the model and gaining insights into how it makes predictions. As a result, DNNs are often considered as black-box models [12]. However, in safety-critical healthcare applications with profound implications for human lives, there is a growing demand to utilise interpretable deep-learning disease diagnosis algorithms that can be effortlessly comprehended and trusted by human experts [12], [13].

Most existing disease diagnosis algorithms attempt to improve model interpretability or transparency with saliency maps that are typically based on post-hoc explanations [14] (e.g., CAM and its variants [15], visual attentions [16], counterfactual example [17], and occlusion sensitivity [18]). However, these methods have many drawbacks, such as: 1) saliency maps only give a spatial importance of image regions related to the model's predictions but they do not explain how those image regions are used for the predictions, which are not enough to interpret the model's inner working [12], [13]; 2) saliency maps could be essentially the same for different classes, as evidenced in [12]; and 3) post-hoc explanations are often unreliable or even misleading since they are not involved in the model's training to penalise explanation errors, unless additional regularisation training objectives [19], [20] are applied to constrain the saliency maps.

These drawbacks are mitigated with model interpretability by prototypical learning [21], [22], as demonstrated in Fig. 1(a), which leverages self-explaining models [23]–[25]. The basic notion behind this strategy is that the model is trained to automatically learn class-specific prototypes (image-level [21], region-level [23], or pixel-level [25], [26]) from training samples. Then, the prediction interpretation is performed by comparing a testing sample with the learned prototypes, which aiding in interpreting the model's inner workings. Such a self-explaining strategy relies on train-test sample associations for decision making, which resembles how humans reason according to cognitive psychological studies [27], [28] revealing that humans use past cases as models when learning to solve problems. Because of this intuitive nature, recent studies successfully leveraged it for single-label classification problems, i.e., diagnosis and interpretation of the breast cancer [29], diabetic retinopathy [30], and Alzheimer's disease [31], where class-specific prototypes are clearly learned from the single-label training samples of the corresponding class. However, the application of the prototype-based interpretation strategy to multi-label classification problems faces critical challenges, mostly due to the complexity of multi-label samples, which inherently intertwine representative disease features from multiple classes. Such

This work was supported in part by funding from the Australian Government under the Medical Research Future Fund - Grant MRFAI000090 for the Transforming Breast Cancer Screening with Artificial Intelligence (BRAIx) Project. (Corresponding author: Chong Wang.)

Chong Wang and Yuanhong Chen are with the Australian Institute for Machine Learning, University of Adelaide, SA 5000, Australia (e-mail: chong.wang@adelaide.edu.au; yuanhong.chen@adelaide.edu.au).

Fengbei Liu is with the Cornell University, New York City, NY 10044, USA (e-mail: fl453@cornell.edu).

Helen Frazer is with the St Vincent's Hospital Melbourne, VIC 3002, Australia (e-mail: helen.frazer@svha.org.au).

Gustavo Carneiro is with the Centre for Vision, Speech and Signal Processing (CVSSP), University of Surrey, United Kingdom, and also with the Australian Institute for Machine Learning, University of Adelaide, SA 5000, Australia (e-mail: g.carneiro@surrey.ac.uk).

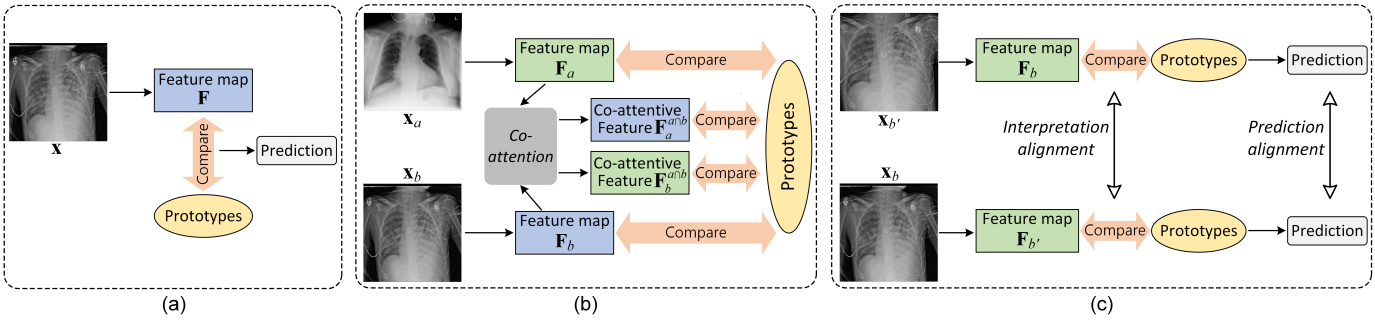

Fig. 1. In multi-label learning, (a) conventional prototypical learning strategy directly learns class prototypes from entangled multiple diseases present in training samples, by considering only individual-image information; (b) our cross-image prototypical learning strategy leverages common semantics of paired images to learn class prototypes from disentangled multiple diseases; (c) our intra-image prototypical learning strategy exploits consistent cues between paired augmented views of an image for regularising both interpretations and predictions.

complexity presents significant obstacles to the effective learning of the class-specific prototypes, resulting in prototypes that are highly entangled with multi-class disease features.

In this paper, we address the problem of multi-label disease diagnosis and interpretation via **C**ross- and **I**ntra-image **P**rototypical **L**earning (**CIPL**). The overall motivation of our CIPL method is illustrated in Fig. 1. Compared with the conventional prototypical learning strategy in Fig. 1(a) that merely learns class prototypes from multi-label training images containing entangled disease features of multiple classes, we propose to leverage the common cross-image semantics of paired images to disentangle the multi-class disease features with a co-attention mechanism, as shown in Fig. 1(b). In this way, our CIPL method enables the class prototypes to gain a comprehensive understanding of pathological lesions for each disease class. Moreover, to obtain robust interpretation and improved classification, our CIPL further exploits consistent and meaningful intra-image cues between different views of an image, as demonstrated in Fig. 1(c). This is achieved through a two-level alignment-based paradigm, which regularises the model interpretations and predictions in a self-supervised fashion. Generally, the cross-image and and intra-image strategies can complementarily contribute to the effective learning of class prototypes from multi-label training samples.

In summary, our main contributions are listed as follows:

1) We present the CIPL method to address the multi-label disease diagnosis and interpretation with prototypical learning. CIPL leverages rich cross-image semantics and consistent intra-image cues to complementarily facilitate the prototype learning from multi-label images.
2) We propose a novel multi-disease disentangling strategy by discovering common cross-image semantics between multi-label samples, enabling the class prototypes to comprehensively understand the pathological lesions.
3) We introduce a new regularisation paradigm based on two-level alignments which exploit consistent intra-image information to promote both interpretation robustness and predictive performance.

Extensive experiments on two public multi-label benchmarks reveal that our CIPL achieves the state-of-the-art (SOTA) disease diagnosis and interpretation results.

II. Related Work

A. Multi-label Disease Diagnosis

From a general domain like computer vision, multi-label classification (MLC) has been studied extensively in various contexts [32]–[35], e.g., handling class label imbalance [32] and exploring dependencies between labels [33]. For example, DB-Focal [32] devises a distribution-balanced loss to tackle the negative-label dominance issue in long-tailed multi-label scenarios. C-Tran [33] adopts a convolutional neural network (CNN) encoder to extract visual features from images and a visual transformer encoder to capture complex dependencies among visual features and labels. CPCL [36] improves classification performance by exploiting the compositional nature of multi-label images through category prototypes.

In recent years, MLC has exhibited widespread use in medical imaging domain for the diagnosis of multi-label diseases, where one of the most common scenarios is thoracic diseases in chest X-rays [37]–[43]. For instance, CheXNet [37] employs a deep dense convolutional network (DenseNet121) for classifying chest radiology, reaching a radiologist-level pneumonia detection performance. MAE [44] further improves the performance by pre-training the DenseNet121 network with modern self-supervised techniques, e.g., masked autoencoder [45]. AnaXNet [46] adopts graph convolutional networks to model dependencies between disease labels as well as relationships between anatomical regions in multi-label chest X-rays. In [16], a hierarchical (i.e., foreground, positive, and abnormality) attention mining method is proposed for multi-label thoracic disease diagnosis and localisation from chest X-ray images. In [38], a multi-modal thoracic disease reasoning framework is developed by harnessing both visual features of X-ray images and graph embeddings of the disease knowledge. MARL [47] presents a deep reinforcement learning framework for chest X-ray classification, enabling the diagnostic agent to be exploratory and contributing to improved classification accuracy. ThoraX-PriorNet [48] exploits both the disease-specific prior and lung region prior as guidance to attend to meaningful anatomical regions for enhanced thorax disease classification. In [49], a framework called TA-DCL, which incorporates triplet attention with dual-pool contrastive learning, is designed for generalised multi-label classification in medical images, including thoracic and ophthalmic diseases. Recent researches [50]–[53] have been shifting towards developing

chest X-ray foundation models based on visual-language pre-training techniques, demonstrating leading performances on some widely-used public benchmarks.

Regardless of their encouraging results, the aforementioned approaches mostly rely on black-box deep-learning models, which produce only a diagnostic outcome with poor interpretability to human users, potentially impeding their successful translation into real-world clinical practice. In contrast, interpretable deep-learning models not only provide the diagnostic prediction, but also elucidate the reasoning behind their decisions. This transparency is highly beneficial for model debugging, as it allows for the analysis of misbehavior when incorrect or unexpected predictions occur [12].

B. Prototypical Learning for Interpretation

The notion of prototypical learning can be traced back to [21] where the seminal prototypical network is designed to learn a metric space in which classification can be made by computing similarities to prototype representations of each class. In [21], the prototypes are image-level since they are estimated as the mean of embedded feature vectors of whole images for each class. Derived from [21], some follow-up studies introduce the idea of prototypical learning for model interpretation in image classification. One important representative is ProtoPNet [23], [54], which automatically learns region-level prototypes to represent object-parts from training images for each class and then realises interpretable reasoning by evaluating similarities between a testing image and the learned training prototypes (prototypical parts). Due to this exemplar-driven nature, some works extend to use pixel-wise prototypes for improving the transparency of semantic segmentation models [22], [25].

Recently, the prototypical learning has been explored for single-label disease diagnosis and interpretation, e.g., diabetic retinopathy grading [30], breast cancer screening [29], [55], and Alzheimer's disease detection [31]. In these single-label tasks, the class-specific prototypes can be readily obtained by directly learning from the single-label training samples of the corresponding class, to capture representative and discriminative visual patterns. However, regarding the more challenging multi-label problem, a training sample is prone to be associated with multiple labels simultaneously. This indicates that the discriminative features of multiple classes are entangled together, undermining the effective learning of class prototypes. To overcome this issue, we propose a cross-image prototype learning strategy with a co-attention mechanism to disentangle the disease features of multiple classes so that the class prototypes can comprehensively represent the pathological lesions of each disease class. In addition, we also present a two-level alignment-based regularisation strategy that leverages consistent intra-image cues to obtain robust interpretation and improved classification.

III. Methodology

We introduce our CIPL method for diagnosis and interpretation of multi-label diseases from medical images. Given a set of training images with image-level labels, CIPL is trained to automatically learn region-level prototypes for each class that encode representative and discriminative visual features, e.g. (pathological lesions or normal tissues). Since we target the multi-label problem, CIPL further makes full use of additional cross- and intra-image information to benefit the learning of class prototypes. During testing, CIPL realises interpretable reasoning by evaluating similarities between a testing image and the class prototypes of training image regions.

Let us denote the training set with $\mathcal{D} = \{(\mathbf{x}_a, \mathbf{y}_a)\}_{a=1}^{|\mathcal{D}|}$, where $\mathbf{x} \in \mathcal{X} \subset \mathbb{R}^{H\times W\times 3}$ is an image of size $H \times W$ and 3 colour channels, $\mathbf{y}_a = [y^1, y^2, ..., y^C]^\top \in \mathcal{Y} \subset \{0,1\}^C$ denotes the image-level class label, where C represents the number of all possible disease labels, and y^c is a binary indicator, i.e., y^c = 1 if the disease of label c is present in the image $\mathbf{x}_a$, and y^c = 0 otherwise. As in conventional MLC, we formulate the multi-disease diagnosis problem with binary classification (one disease vs. no-findings/normal) for each of the C disease labels. In other words, our CIPL achieves interpretable multi-label predictions by comparing a testing image with prototypes of each disease class as well as those of the no-findings class. If there are multiple disease classes where the similarities with their respective class prototypes are larger than that of the no-findings class, the testing image will be classified with all these multiple disease labels.

A. Method Overview

An overview of our CIPL is shown in Fig. 2, where training image pairs, represented with $\mathbf{x}_a$, $\mathbf{x}_b$, are sampled from $\mathcal{D}$ and then fed into the same feature backbone $f_{\theta_f} : \mathcal{X} \rightarrow \mathcal{F}$ (parameterised by θ_f) to extract the feature maps $\mathbf{F}_a, \mathbf{F}_b \in \mathcal{F} \subset \mathbb{R}^{\bar{H}\times\bar{W}\times D}$, with D denoting the feature dimension, and usually $\bar{H} < H$, $\bar{W} < W$. Following the general protocol of prototypical learning [23], [24], [29], a prototype layer $\varphi_{\mathcal{P}} : \mathcal{F} \rightarrow \mathcal{S}$ learns $N = M(C+1)$ class-specific prototypes $\mathcal{P} = \{\mathbf{p}^n\}_{n=1}^N$, with M prototypes per class (including no-findings) and $\mathbf{p}^n \in \mathbb{R}^{1\times 1\times D}$, as shown in Fig. 2(b). The prototype layer computes similarity maps $\mathbf{S}_a$, $\mathbf{S}_b \in \mathcal{S} \subset \mathbb{R}^{\bar{H}\times\bar{W}\times N}$ between the feature maps $\mathbf{F}_a$, $\mathbf{F}_b$ and prototypes $\mathcal{P}$, e.g., $\mathbf{S}_a^{n,(i,j)} = \exp^{-||\mathbf{F}_a^{(i,j)} - \mathbf{p}^n||_2^2/D}$ for $\mathbf{F}_a$, where $i \in \{1, ..., \bar{H}\}$ and $j \in \{1, ..., \bar{W}\}$ are spatial indexes. Due to the class-specific property of prototypes, the similarity maps $\mathbf{S}_a$, $\mathbf{S}_b$ can be viewed as class-wise prototypical activation maps, which are reduced to represent N similarity scores using max-pooling, e.g., $\mathbf{s}_a^n = \max_{(i,j)} \mathbf{S}_a^{n,(i,j)}$ for $\mathbf{S}_a$. These N similarity scores for each image are fed to a fully-connected (FC) layer $g_{\theta_g} : \mathbb{R}^N \rightarrow \mathbb{R}^{C+1}$ to generate $C+1$ classification scores (logits). Given the multi-label problem, we reorganise the logits to produce C binary tasks, with each of them corresponding to one disease vs. no-findings. Finally, a softmax function is employed to derive the C binary probabilistic predictions $\widehat{\mathbf{y}}_a, \widehat{\mathbf{y}}_b \in \mathbb{R}^{C\times 2}$. The basic training objective of our CIPL method is defined as follows:

$$\mathcal{L}_{basic} = \ell_{ce}(\widehat{\mathbf{y}}_a, \mathbf{y}_a) + \ell_{ce}(\widehat{\mathbf{y}}_b, \mathbf{y}_b) + \alpha_1(\mathcal{L}_{cst} + \mathcal{L}_{sep}), \quad (1)$$

where $\ell_{ce}(\cdot)$ is the cross-entropy loss, α_1 is a weighting factor for the two commonly-used auxiliary losses [23], [24], [29],

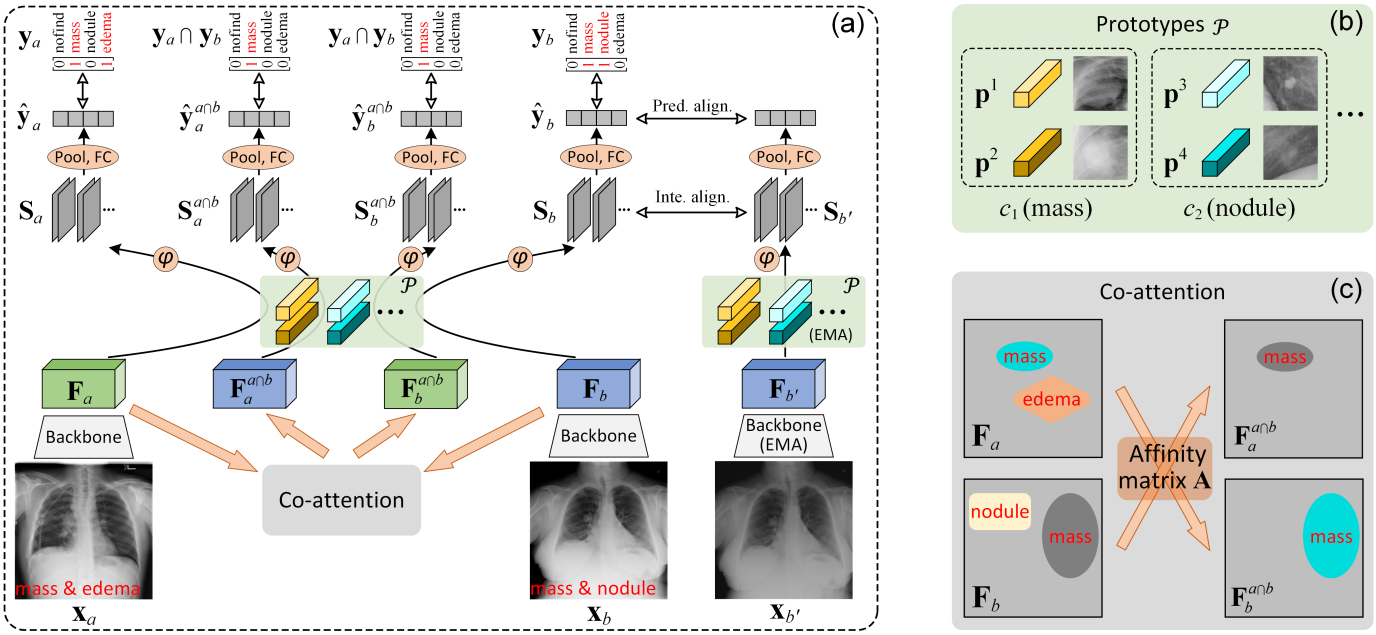

Fig. 2. (a) Architecture of our proposed CIPL method for the multi-label disease diagnosis and interpretation. CIPL leverages a co-attention mechanism to mine cross-image semantics from paired images $\mathbf{x}_a$ and $\mathbf{x}_b$, with the goal of learning disentangled class prototypes from multi-label training samples. CIPL also regularises the prototype's learning with interpretation and prediction consistency between augmented image views, e.g., $\mathbf{x}_b$ and $\mathbf{x}_{b'}$; (b) examples of prototypes that encode representative pathological lesions for each disease class (here we illustrate two prototypes per class); (c) co-attention mechanism extracts common semantics between paired images for multi-class disease disentangling.

i.e., clustering $\mathcal{L}_{cst}$ and separation $\mathcal{L}_{sep}$:

$$\mathcal{L}_{cst} = \min_{\mathbf{p}^n \in \mathcal{P}_{\mathbf{y}_a}} \min_{\mathbf{f} \in \mathbf{F}_a} ||\mathbf{f} - \mathbf{p}^n||_2^2 + \min_{\mathbf{p}^n \in \mathcal{P}_{\mathbf{y}_b}} \min_{\mathbf{f} \in \mathbf{F}_b} ||\mathbf{f} - \mathbf{p}^n||_2^2, \quad (2)$$

$$\mathcal{L}_{sep} = \max\left(0, \tau - \min_{\mathbf{p}^n \notin \mathcal{P}_{\mathbf{y}_a}} \min_{\mathbf{f} \in \mathbf{F}_a} ||\mathbf{f} - \mathbf{p}^n||_2^2\right) + \max\left(0, \tau - \min_{\mathbf{p}^n \notin \mathcal{P}_{\mathbf{y}_b}} \min_{\mathbf{f} \in \mathbf{F}_b} ||\mathbf{f} - \mathbf{p}^n||_2^2\right). \quad (3)$$

Taking the training image $\mathbf{x}_a$ as an example, the clustering loss $\mathcal{L}_{cst}$ in Eq. (2) ensures the image contains at least one local feature vector $\mathbf{f} \in \mathbb{R}^{1\times1\times D}$ in $\mathbf{F}_a$ that is close to one of the prototypes of its own class (denoted by the set $\mathcal{P}_{\mathbf{y}_a}$), while the separation loss $\mathcal{L}_{sep}$ in Eq. (3) forces all feature vectors of $\mathbf{F}_a$ to stay distant (with a positive margin τ) from the prototypes that belong to other classes.

Until now, our CIPL follows the conventional training strategy as in current approaches (e.g., ProtoPNet [23]) that only consider individual-image information for prototype learning. However, a challenge arises due to the entanglement of multi-class disease features in multi-label samples, which significantly hinders the effective learning of the class prototypes. To handle this issue, we describe in Section III-B how our CIPL additionally mines cross-image semantics via a co-attention mechanism to facilitate the disentanglement of disease features from multiple classes, enabling the prototypes to have a more precise and comprehensive understanding of various pathological lesion patterns. Meanwhile, we further present a two-level alignment-based strategy that regularises the prototype learning by exploiting consistent intra-image information, as elaborated in Section III-C.

B. Cross-image Prototypical Learning via Co-attention

In multi-label diagnosis problems, label co-occurrence usually leads to the entanglement of features associated with multiple diseases, which is the primary obstacle for the effective learning of class-specific prototypes from multi-label samples. In this section, we propose a solution to decouple these entangled features with the goal of improving the learning of class prototypes in multi-label problems. To achieve this, we leverage the well-established co-attention technique [56]–[58] to take advantage of cross-image information. The co-attention has been shown to be effective in capturing underlying relationships between different entities, e.g., vision-language navigation [59] and video segmentation [57]. Motivated by the general idea of co-attention mechanisms, our CIPL method harnesses it to discover common semantics within pairs of training images, which enhances the multi-disease feature disentanglement and allows the class prototypes to capture visual patterns of complicated pathological lesions.

As illustrated in Fig. 2(a), our CIPL method attends to image pairs, i.e., $\mathbf{x}_a$, $\mathbf{x}_b$, in the feature space, where the two images share at lease one common label, denoted by $\mathbf{y}_a \cap \mathbf{y}_b$. Specifically, we first transform $\mathbf{F}_a$ and $\mathbf{F}_b$ into matrices denoted by $\bar{\mathbf{F}}_a$ and $\bar{\mathbf{F}}_b \in \mathbb{R}^{\bar{H}\bar{W}\times D}$, and employ them to calculate an affinity matrix $\mathbf{A} \in \mathbb{R}^{\bar{H}\bar{W}\times\bar{H}\bar{W}}$, with each entry computed as follows:

$$\mathbf{A}^{i,j} = \mathsf{sim}(\bar{\mathbf{F}}_a^i, \bar{\mathbf{F}}_b^j) = -||\bar{\mathbf{F}}_a^i - \bar{\mathbf{F}}_b^j||_2^2, \quad (4)$$

where $\bar{\mathbf{F}}_a^i$ and $\bar{\mathbf{F}}_b^j$ denote a D-dimensional feature vector in $\bar{\mathbf{F}}_a$ and $\bar{\mathbf{F}}_b$ at position i and j, respectively. It is worth mentioning that our CIPL utilises the negative L_2 distance as the similarity metric $\mathsf{sim}(\cdot)$, since it is also used to measure the similarity between the feature maps and prototypes (see Section III-A). This differs from the standard co-attention strategy [56], [57] demanding an additional trainable parameter in computing the affinity matrix. Based on Eq. (4), we can apply a column-wise

softmax operation on $\mathbf{A}$ to obtain the co-attention weights:

$$\mathbf{W}_a = \text{softmax}(\mathbf{A}) \in [0,1]^{\bar{H}\bar{W}\times\bar{H}\bar{W}}, \tag{5}$$

$$\mathbf{W}_b = \text{softmax}(\mathbf{A}^\top) \in [0,1]^{\bar{H}\bar{W}\times\bar{H}\bar{W}}. \tag{6}$$

Next, the attention summary for the feature representation $\bar{\mathbf{F}}_a$ (or $\bar{\mathbf{F}}_b$) with respect to $\bar{\mathbf{F}}_b$ (or $\bar{\mathbf{F}}_a$) are given by:

$$\bar{\mathbf{F}}_a^{a\cap b} = \bar{\mathbf{F}}_b\mathbf{W}_b \in \mathbb{R}^{D\times\bar{H}\bar{W}}, \tag{7}$$

$$\bar{\mathbf{F}}_b^{a\cap b} = \bar{\mathbf{F}}_a\mathbf{W}_a \in \mathbb{R}^{D\times\bar{H}\bar{W}}. \tag{8}$$

The above two co-attentive features are then reshaped to restore their spatial dimensions, i.e., $\mathbf{F}_a^{a\cap b}$ and $\mathbf{F}_b^{a\cap b} \in \mathbb{R}^{\bar{H}\times\bar{W}\times D}$, which are supposed to preserve the common semantics between $\mathbf{F}_a$ and $\mathbf{F}_b$ and focus on the shared object regions (e.g., pathological lesions of the same disease class) in both $\mathbf{x}_a$ and $\mathbf{x}_b$. In this way, the class-aware disentangled features can be favourably extracted (see Fig. 2(c)), benefiting the learning of class prototypes. Therefore, the co-attentive features are incorporated into the prototype layer $\varphi_{\mathcal{P}}(\cdot)$ by comparing with the prototypes in $\mathcal{P}$, whose prediction outputs are supervised with the common labels $\mathbf{y}_a \cap \mathbf{y}_b$:

$$\begin{aligned}\mathcal{L}_{cross} = \ell_{ce}\big(g_{\theta_g}(\varphi_{\mathcal{P}}(\mathbf{F}_a^{a\cap b})), \mathbf{y}_a\cap\mathbf{y}_b\big) + \\ \ell_{ce}\big(g_{\theta_g}(\varphi_{\mathcal{P}}(\mathbf{F}_b^{a\cap b})), \mathbf{y}_a\cap\mathbf{y}_b\big).\end{aligned} \tag{9}$$

Consider the illustration in Fig. 2, where *mass* and *edema* exist in $\mathbf{x}_a$, while *mass* and *nodule* are present in $\mathbf{x}_b$. Since the co-attention is essentially performed among all the feature position pairs between $\mathbf{x}_a$ and $\mathbf{x}_b$, only the disease with common semantics, *mass*, is preserved in the co-attentive features $\mathbf{F}_a^{a\cap b}$ and $\mathbf{F}_b^{a\cap b}$. When using the common label, *mass*, as the supervisory signal, the *mass* prototypes will be uniquely associated with the corresponding disentangled features of *mass* regions to comprehensively and accurately understand the pathological *mass* lesions. From an another viewpoint, the co-attention across the two related images enables our CIPL to become aware that the semantics preserved in $\mathbf{x}_a$ and $\mathbf{x}_b$ are relevant and can be exploited to jointly learn effective prototypes for identifying the *mass* disease. It essentially takes advantage of the context across training data.

Apart from the co-attention based prototypical learning strategy that exploits the relevant cross-image semantics, we further develop an alignment-based prototypical learning paradigm that mines consistent and useful intra-image cues between different views of a training image, introduced in the following Section III-C. The cross-image and intra-image strategies provide a complementary way to help the model to obtain effective prototypes from multi-label samples.

C. Intra-image Prototypical Learning via Alignment

Inherited from the strengths of existing prototype-based approaches, our proposed CIPL method not only offers classification predictions for disease diagnosis but also furnishes a promising interpretable reasoning through the presentation of a set of similarity maps. These maps are associated with disease-representative prototypes derived from training images, providing a transparent process of disease interpretation. In order to promote interpretation robustness and predictive performance, we present a self-supervised alignment-based method which regularises both the prototype learning and model predictions by exploiting consistent and meaningful intra-image information between image views.

In line with popular self-supervised learning techniques [60], we adopt two different views, denoted by $\mathbf{x}_b, \mathbf{x}_{b'}$, augmented from the same training image, as demonstrated in Fig. 2(a). Since our CIPL achieves model interpretations through the similarity maps with training prototypes, we propose to leverage the intra-image cues by enforcing interpretation consistency between the two input views. This is formulated as the spatial alignment between the similarity maps $\mathbf{S}_b$ and $\mathbf{S}_{b'}$ from the two image views, as follows:

$$\mathcal{L}_{inte}(\mathbf{x}_b, \mathbf{x}_{b'}) = -\frac{1}{\bar{H}\bar{W}}\sum_{(i,j)\in\bar{H}\times\bar{W}} h(\mathbf{S}_b^{:,(i,j)}, \mathbf{S}_{b'}^{:,(i,j)}), \tag{10}$$

where $h(\cdot)$ computes the cosine similarity. In Eq. (10), our CIPL is driven to produce robust prototypes to pathological lesions characterised by varying structures and appearances.

In addition to the interpretation alignment, we also propose to enhance alignment with respect to the classification predictions between the two image views, where one straightforward solution is to minimise KL-divergence of probabilistic predictions from the two views, for each individual training sample. However, we experimentally notice that such a solution does not lead to a notable improvement in predictive performance (detailed in our experiments). Consequently, we design a new batch-level alignment strategy by further considering sample relationships, which is formulated as:

$$\mathcal{L}_{pred}(\mathcal{B}, \mathcal{B}') = \frac{1}{C\cdot|\mathcal{B}|^2}\sum_{c=1}^{C}||\mathbf{G}^c - \mathbf{G}^{c,\prime}||_2^2, \tag{11}$$

where $\mathcal{B}$ and $\mathcal{B}'$ denote two independent mini-batches with size $|\mathcal{B}| = |\mathcal{B}'|$, $\mathbf{G}^c$ and $\mathbf{G}^{c,\prime} \in \mathbb{R}^{|\mathcal{B}|\times|\mathcal{B}|}$ represent the class-wise Gram matrix that measures the prediction correlations between samples within mini-batches $\mathcal{B}$ and $\mathcal{B}'$, respectively, which are given by:

$$\mathbf{G}^c = \widehat{\mathbf{Y}}^c\cdot(\widehat{\mathbf{Y}}^c)^\top, \mathbf{G}^{c,\prime} = \widehat{\mathbf{Y}}^{c,\prime}\cdot(\widehat{\mathbf{Y}}^{c,\prime})^\top, \tag{12}$$

with $\widehat{\mathbf{Y}} = [\widehat{\mathbf{y}}_1, \widehat{\mathbf{y}}_2, ..., \widehat{\mathbf{y}}_{|\mathcal{B}|}], \widehat{\mathbf{Y}}' = [\widehat{\mathbf{y}}_1', \widehat{\mathbf{y}}_2', ..., \widehat{\mathbf{y}}_{|\mathcal{B}'|}] \in \mathbb{R}^{|\mathcal{B}|\times C\times 2}$ denoting probabilistic predictions of all training samples of mini-batches $\mathcal{B}$ and $\mathcal{B}'$, respectively. Note that in Eq. (11) and (12) we omit notations b, b', defining different views of the same image, to keep definitions uncluttered.

In order to enable a stable training, we employ the well-known momentum update technique [61] to form an exponential moving average (EMA) model, $\theta_{\text{ema}}^{t+1} := \lambda\theta_{\text{ema}}^t + (1-\lambda)\theta^t$, where $\lambda = 0.999$ is the momentum coefficient. During training, one image view (such as $\mathbf{x}_b$) is fed to the current model, and another view $\mathbf{x}_{b'}$ to the EMA model. The EMA model can be discarded once the training completes.

D. Overall Training Objectives

We have introduced all training components of our CIPL method for multi-label disease diagnosis and interpretation. The overall training objective is expressed as follows:

$$\mathcal{L}_{total} = \mathcal{L}_{basic} + \alpha_2\mathcal{L}_{cross} + \alpha_3\mathcal{L}_{inte} + \alpha_4\mathcal{L}_{pred}, \tag{13}$$

where α_2, α_3, and α_4 are trade-off factors for the corresponding loss terms.

To enable all prototypes in $\mathcal{P}$ to be represented by actual training image patches, we replace each prototype $\mathbf{p}^n$ with the nearest training patch feature of the corresponding class [23], [24], after each training epoch, with:

$$\mathbf{p}^n \leftarrow \arg \min_{\mathbf{f} \in \mathbf{F}_{a \in \{1,2,\ldots,|\mathcal{D}|\}}} ||\mathbf{f} - \mathbf{p}^n||_2^2. \tag{14}$$

This step ensures the transparency of the prototypes (i.e., grounding them in the human-understandable image space), so that the case-based interpretability is achieved by classifying testing images based on their similarities to the training prototypes of image patches. To facilitate the richness and diversity of visual patterns captured by the prototypes, in Eq. (14) we adopt the greedy prototype replacement strategy [29], guaranteeing that all prototypes are derived from entirely distinctive (non-repetitive) training images. To be specific, if duplicate prototypes are observed, the next most-similar training image patch is used in the replacement instead. Additionally, Eq. (14) is also employed to visualise the learned class prototypes (see Fig. 3 in Section IV), as in [23], [24].

Compared with the conventional prototypical learning approaches [23], [24], [29] designed for single-label problems, our CIPL method does not introduce any excessive learnable network parameters. During the training phase, CIPL incurs a moderate increase in computational overhead due to computation of the affinity matrix, but it does not require additional computational resources in the test phase.

IV. Experiments

A. Data Sets

In this work, we utilise two public benchmark datasets to validate the effectiveness of our proposed CIPL method for multi-label diagnosis and interpretation, namely the thoracic diseases on NIH ChestX-ray14 [62] and ophthalmic diseases on Ocular Disease Intelligent Recognition (ODIR) [63].

The multi-label NIH ChestX-ray14 dataset [62] consists of 112,120 chest X-ray images featuring 14 labels of thoracic diseases as well as a "no-findings" label, acquired from 30,805 patients. In ChestX-ray14, 880 images are annotated with 984 bounding boxes, specifying the disease regions across 8 disease categories. In our experiment, the original X-rays are resized to $H = W = 512$, and we use ChestX-ray14 for both classification and weakly-supervised localisation of thoracic diseases. *Disease Classification:* our experimental setup strictly adheres to the official train/test split in [62]. The classification results are evaluated using the AUC, F1 score, and accuracy, where we follow the previous studies [51], [52] to determine the thresholds in calculating the mean F1 score and accuracy. *Weakly-supervised Disease localisation:* we average the class activation maps and produce a binary localisation mask with a threshold 0.5 for a disease class. In alignment with previous localisation approaches [16], [64] that rely on only image-level training labels, our method is trained on all 111,240 images without any box annotations. Testing is then performed on the remaining 880 images that have box annotations. The localisation performance is assessed using the thresholded IoU accuracy [16], defined as the ratio of correctly localised cases to the total cases for each disease class. Correct localisation is determined by the IoU score between the predicted and ground-truth localisation masks, which should exceed a predefined IoU threshold T(IoU).

ODIR [63] is a public database of colour fundus images containing multi-label ophthalmic diseases. In ODIR, there are a total of 10,000 images from left and right eyes of 5,000 patients. The labels are provided for each patient, including normal, diabetes, glaucoma, cataract, aged-macular degeneration (AMD), hypertension, myopia, and other diseases. ODIR also offers detailed diagnostic keywords related to each fundus image, allowing to relabel the images and perform an eye-level classification. In this work, we employ the relabelling procedure in [65] to realise eye-level diagnosis. Our experiments follow the official train/test split [63], where the whole ODIR is divided into train set (6970 images), on-site test set (1972 images), and off-site test set (991 images), after excluding low-quality images (e.g., lens dust, image offset, and invisible optic disk), as in [63], [65]. Original fundus images undergo an automatic circular border cropping process, followed by resizing to $H = W = 640$ as model input. We report the AUC, F1 score, and accuracy metrics to evaluate the classification performance.

B. Experimental Settings

Our proposed method adopts CNN-type feature backbone f_{θ_f} (DenseNet-121 [71] for chest X-rays and ResNet101 [72] for fundus images), which are pre-trained on ImageNet, as in mainstream previous works. To enable rigorous model evaluation, we utilise purely official train/test data provided by both datasets, without introducing any additional data or test-time augmentation, as suggested in [73]. Typically, input images are down-sampled 32 times by the backbone f_{θ_f}, so $\bar{H} = \frac{H}{32}$ and $\bar{W} = \frac{W}{32}$. We have the feature dimension $D = 256$ by appending two 1×1 convolutional layers after f_{θ_f} (one activated by ReLU and the other activated by Sigmoid). For both tasks, we adopt $M = 50$ prototypes per class, so $N = 750$ and 400 for X-rays and fundus images, respectively. Our CIPL is implemented with PyTorch platform and trained using the Adam optimiser with mini-batch sizes $|\mathcal{B}| = |\mathcal{B}'| = 24$ and initial learning rate of 10^{-4}, decreased by a rate of 0.5 per 5 epochs after reaching a steady performance. In Eq. (3), we have the margin $\tau = 2$. The weighting factors in Eq. (1) and Eq. (13) are set as $\alpha_1 = 0.02$, $\alpha_2 = \alpha_3 = \alpha_4 = 0.5$. We first train our CIPL for 15 epochs using only $\mathcal{L}_{basic}$ in Eq. (1) to warm-up the model, then we use the overall objective $\mathcal{L}_{total}$ in Eq. (13) to train the model for 40 epochs. Our method undergoes five runs with different random initialisation seeds, from which the results are reported.

In Section III-C, our intra-image prototypical learning strategy relies on two augmented image views $\mathbf{x}_b$ and $\mathbf{x}_{b'}$. However, the two views should not have spatially drastic disparities, since Eq. (10) enforces the interpretation alignment of similarity maps at the spatial level. To this end, we devise a two-step augmentation scheme. The first step applies basic location-oriented transformations, encompassing scaling, shearing, rotation, translation, and flipping, to increase the

TABLE I
QUANTITATIVE THORACIC DISEASE CLASSIFICATION RESULTS ON NIH CHESTX-RAY14, REPORTED WITH THE AUC ON THE 14 DISEASES, MEAN AUC (MAUC), MEAN F1 (MF1), AND MEAN ACCURACY (MACC) METRICS. TOP-PART ILLUSTRATES GENERAL CLASSIFICATION METHODS AND BOTTOM PART ILLUSTRATES PROTOTYPE-BASED APPROACHES, WITH BEST RESULTS HIGHLIGHTED IN BOLD. * WE RE-TRAIN THE MODEL ON OFFICIAL DATA SPLIT FOR FAIR COMPARISON, USING THE AUTHOR'S OFFICIALLY RELEASED ALGORITHMS.

Method	Atel	Card	Effu	Infi	Mass	Nodu	Pnea	Pnex	Cons	Edem	Emph	Fibr	P.T.	Hern	mAUC	mF1	mACC
Wang *et al.* [62]	0.700	0.810	0.759	0.661	0.693	0.669	0.658	0.799	0.703	0.805	0.833	0.786	0.684	0.872	0.745		
Guendel *et al.* [66]	0.772	0.881	0.826	0.710	0.824	0.756	0.728	0.851	0.751	0.841	0.897	0.819	0.757	0.901	0.807		
GREN [67]	0.776	0.882	**0.851**	0.660	0.813	0.721	0.675	0.873	**0.790**	**0.893**	0.920	0.795	0.790	0.867	0.807		
ConVIRT [50]	0.771	0.867	0.825	0.703	0.818	0.761	0.722	0.857	0.747	0.854	0.901	0.809	0.771	0.909	0.808		
CheXNet [37]	0.764	0.867	0.819	0.700	0.824	0.775	0.710	0.867	0.746	0.854	0.922	0.821	0.781	0.921	0.814	n/a	n/a
MedKLIP [51]	0.777	0.885	0.827	0.690	0.829	0.771	0.733	0.852	0.748	0.845	0.904	0.821	0.780	0.940	0.815		
Guan *et al.* [68]	0.781	0.883	0.831	0.697	0.830	0.764	0.725	0.866	0.758	0.853	0.911	0.826	0.780	0.918	0.816		
Ma *et al.* [3]	0.777	0.894	0.829	0.696	**0.838**	0.771	0.722	0.862	0.750	0.846	0.908	0.827	0.779	0.934	0.817		
AnaXNet [46]	0.774	0.889	0.824	0.709	0.825	0.776	0.712	0.870	0.751	0.855	0.934	0.820	0.788	0.924	0.818		
CPCL [36]	0.777	0.866	0.832	0.702	0.829	0.792	0.733	0.868	0.747	0.853	0.935	0.840	0.796	0.907	0.820±0.002	0.344±0.003	0.864±0.002
TA-DCL [49]	0.773	0.885	0.825	0.699	0.826	0.788	**0.734**	0.877	0.744	0.849	0.932	0.829	0.795	0.935	0.821±0.002	0.350±0.002	0.868±0.001
MARL* [47]	0.777	0.869	0.833	0.703	0.831	0.794	0.732	0.870	0.750	0.853	0.936	0.838	0.798	0.907	0.821±0.001	0.352±0.001	0.872±0.002
MAE [44]	0.770	0.876	0.824	0.718	0.828	0.771	0.732	0.880	0.745	0.862	0.940	0.831	0.785	0.940	0.822±0.002	0.356±0.002	0.872±0.002
ThoraX-PriorNet* [48]	0.779	0.870	0.833	0.705	0.834	0.794	0.740	0.872	0.748	0.854	0.936	0.845	**0.799**	0.908	0.823±0.001	0.358±0.001	0.873±0.001
KAD [52]	**0.785**	**0.897**	0.840	0.713	0.836	0.771	0.740	0.874	0.753	0.860	0.916	0.829	0.778	**0.961**	0.825	0.364	0.875
ProtoPNet [23]	0.761	0.861	0.810	0.701	0.820	0.783	0.712	0.872	0.743	0.836	0.936	0.801	0.780	0.912	0.809±0.002	0.326±0.002	0.830±0.003
ProtoPNet++ [29]	0.772	0.880	0.828	0.702	0.827	0.786	0.710	0.871	0.741	0.844	0.941	0.823	0.782	0.923	0.816±0.001	0.338±0.002	0.855±0.001
Deformable [24]	0.769	0.878	0.834	0.706	0.824	0.790	0.707	0.872	0.744	0.837	0.943	0.820	0.785	0.929	0.817±0.001	0.341±0.001	0.859±0.002
PIP-Net [69]	0.770	0.876	0.831	0.718	0.823	0.778	0.725	0.880	0.751	0.849	0.939	0.823	0.786	0.915	0.819±0.002	0.347±0.002	0.867±0.002
XProtoNet [70]	0.780	0.887	0.835	0.710	0.831	**0.804**	**0.734**	0.871	0.747	0.840	0.941	0.815	**0.799**	0.909	0.822	n/a	n/a
CIPL	0.776	0.882	0.834	**0.722**	0.830	0.795	**0.734**	**0.883**	0.755	0.859	**0.946**	**0.832**	0.795	0.947	**0.828**±0.001	**0.383**±0.002	**0.885**±0.001

TABLE II
P-VALUES COMPUTED FROM ONE-SIDED PAIRED T-TEST BETWEEN OUR CIPL AND OTHER COMPETING APPROACHES ON NIH CHESTX-RAY14, EVALUATED WITH THE MEAN AUC SCORE.

ProtoPNet [23]	ProtoPNet++ [29]	Deformable [24]	PIP-Net [69]	CPCL [36]	TA-DCL [49]	MARL [47]	MAE [44]	ThoraX-PriorNet [48]	KAD [52]
4.9e-13	1.7e-7	1.9e-6	9.7e-6	3.8e-5	8.9e-5	1.1e-4	4.6e-4	9.0e-4	9.8e-3

diversity of the training set. This augmented image serves as input to the next step, which applies colour-oriented transformations, involving changes in contrast, brightness, sharpness, and hue. To introduce even more variations between the two views, we also use a random crop of size 95% to 100% of the input, with aspect ratio between 0.95 and 1.05. In this way, slight location variations are further incorporated between the two views, but pathological lesions at a specific location will roughly correspond to the same region in both views, and this can therefore help obtain consistent and robust prototypes. It is worthy noticing that the augmentations should preserve key semantic features of the images while avoiding excessive alterations which could distort the underlying class characteristics. Hence, we conduct a series of experiments by varying the strength of the used augmentations, where we apply the augmentations to the training images and monitor the model's performance on the test set. The optimal set of augmentations is determined based on the best observed performance. Our code will be made publicly available, from which more augmentation details can be found[1].

C. Competing Methods

Chest X-ray Classification: we first compare with existing leading multi-label X-ray classification approaches [3], [16], [37], [44], [46]–[52], [62], [66], [67], which are introduced in Section II-A. Furthermore, we also compare with state-of-the-art interpretable approaches that are based on prototypes primarily designed for single-label tasks: ProtoPNet [23], XProtoNet [70], ProtoPNet++ [29], Deformable ProtoPNet [24], and PIP-Net [69]. ProtoPNet [23] is the original work that utilises region-level prototypes for interpretable image classification, and severs as the baseline on which our CIPL is established. Relying on ProtoPNet, XProtoNet [70] further integrates prototypes with disease occurrence maps. ProtoPNet++ [29] presents a two-branch approach ensembling the ProtoPNet with a non-interpretable global deep-learning classifier. Deformable ProtoPNet [24] uses spatially-flexible prototypes to adaptively capture variations of object features from natural images. PIP-Net [69] first pre-trains class-agnostic prototypes and then regularises the prototype-class connection sparsity for compact classification interpretations.

Fundus Image Classification: considering the limited research on multi-label ophthalmic disease diagnosis from fundus images, we begin by comparing our work with the following general multi-label image classification methods: DB-Focal [32], C-Tran [33], CPCL [36], and TA-DCL [49], which are elaborated in Section II-A. In addition, we also compare with the advanced prototype-based interpretable approaches introduced above: ProtoPNet [23], ProtoPNet++ [29], Deformable ProtoPNet [24], and PIP-Net [69].

D. Multi-label Disease Classification and Interpretation

Table I shows thoracic disease classification results of our CIPL and other competing approaches on NIH ChestX-ray14. As can be observed, our CIPL method achieves the best classification results among all these approaches with a mean AUC of 0.828, a mean F1 score of 0.383, and a mean accuracy of 0.885, and it reaches the highest AUC results on five thoracic diseases. Compared with the seminal work of ProtoPNet baseline [23], our CIPL exhibits a large

[1]https://github.com/cwangrun/CIPL

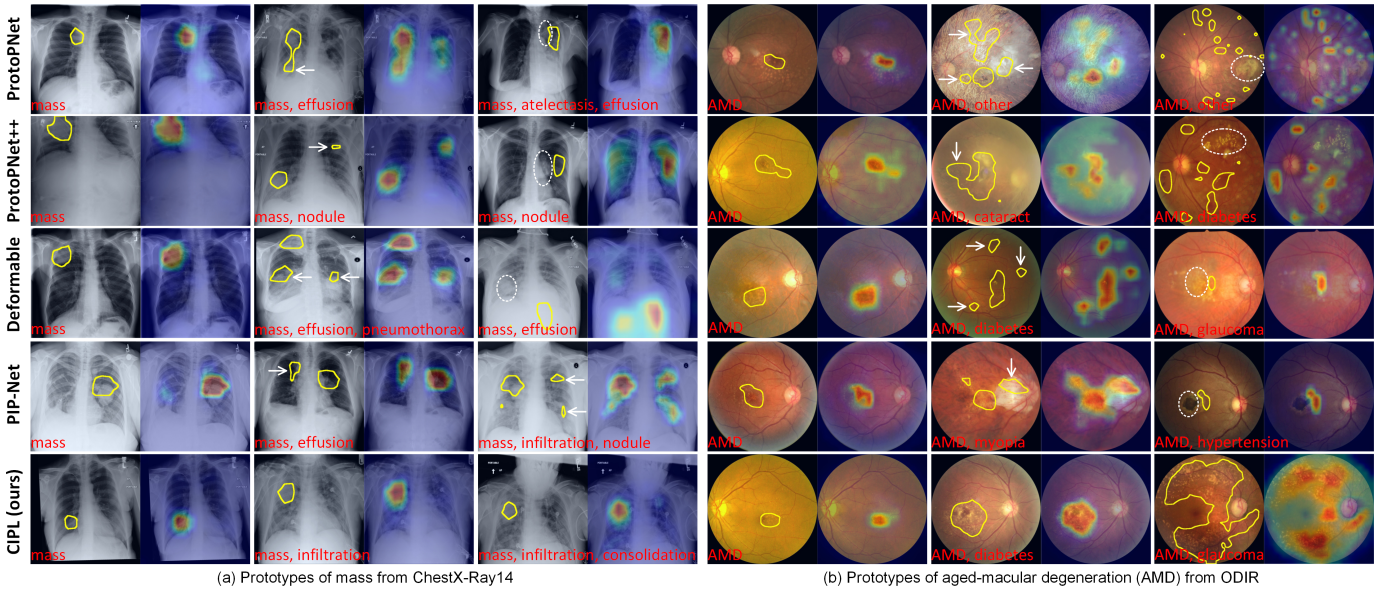

Fig. 3. Visual comparison of prototypes learned from ProtoPNet [23], ProtoPNet++ [29], Deformable ProtoPNet [24], PIP-Net [69], and our CIPL. In each pair, the left-sided image displays the prototype (denoted by yellow counters) in the source training image and the corresponding right-sided image highlights prototypes in the self-activated similarity map. The ground-truth image labels are written in red.

average AUC improvement from 0.809 to 0.828. Notice that our method also greatly surpasses other more advanced interpretable prototypical learning approaches [24], [29], [69], [70], verifying the advantage of CIPL in exploiting cross- and intra-image information with prototypical learning for multi-label classification. Furthermore, our CIPL outperforms the current SOTA chest X-ray classification methods that rely on black-box deep neural networks, such as ThoraX-PriorNet [48], MARL [47], MAE [44], and TA-DCL [49]. Promisingly, our CIPL method exceeds the recent visual-language models (e.g., ConVIRT [50], MedKLIP [51], and KAD [52]), which are even pre-trained on image-text pairs from the large MIMIC-CXR [74] database and further fine-tuned on ChestX-ray14. These results highlight our method's strength of providing accurate diagnosis and interpretation results for thoracic diseases. Table II provides a statistical analysis of our proposed CIPL with respect to other advanced competing approaches using the one-sided paired T-test. All these approaches undergo inference on ChestX-ray14 test set with 1000 bootstrap replicates. We can see that the performance improvements (in mean AUC) of our CIPL over the other considered approaches are statistically significant, with a significance level of 0.05.

Fig. 3(a) provides a visual comparison of typical *mass* prototypes learned by different prototype-based methods. It can be seen that, although obtaining good *mass* prototypes from single-label training samples, the previous prototype-based methods can undesirably generate *mass* prototypes that simultaneously activate *mass* and other diseases (e.g., *effusion* highlighted with the white arrow in the 2nd case, at the top row), showing the phenomena of entangled prototypes. Also, the previous methods tend to produce inaccurate prototypes which are even not aligned with the actual *mass* region (e.g., the white ellipse in the 3rd case, at the top row), due to the disturbance of other diseases in multi-label training samples.

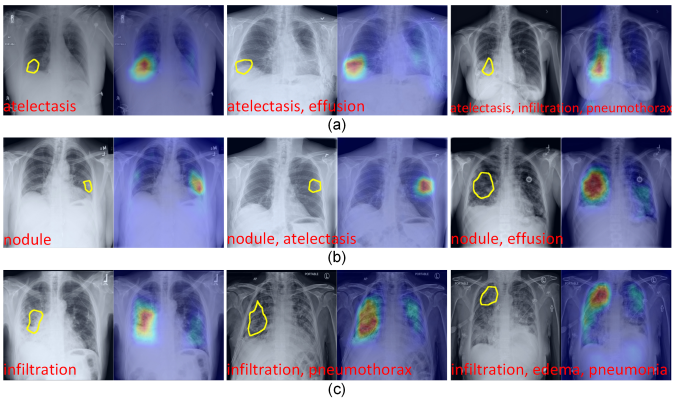

Fig. 4. Visual prototypes of *atelectasis* (a), *nodule* (b), and *infiltration* (c), learned by our CIPL method from NIH ChestX-ray14. In each pair, the left-sided image displays the prototype (denoted by yellow counters) in the source training image and the corresponding right-sided image highlights prototypes in the self-activated similarity map. The ground-truth image labels are written in red.

By contrast, our CIPL successfully obtains disentangled and correct prototypes from both single- and multi-label samples. We further provide visual prototypes of more other thoracic disease classes learned by our proposed CIPL method in Fig. 4, showing their high disentanglement property.

In Fig. 5, we display an example of multiple disease thoracic diagnosis interpretation from a testing chest X-ray image. As evident, our CIPL compares the input image with the learned class prototypes in the feature space, resulting in a series of similarity maps for each disease class and no-findings. The classification logits are generated by summing the weighted maximum similarity scores of the corresponding class. In this example, since the classification logits of *infiltration* and *mass* are higher than that of *no-findings*, our model forms a disease diagnosis outcome of *infiltration* and *mass* from the image. It is worth noting that our model activates the corresponding disease regions that are well-aligned with the manual disease

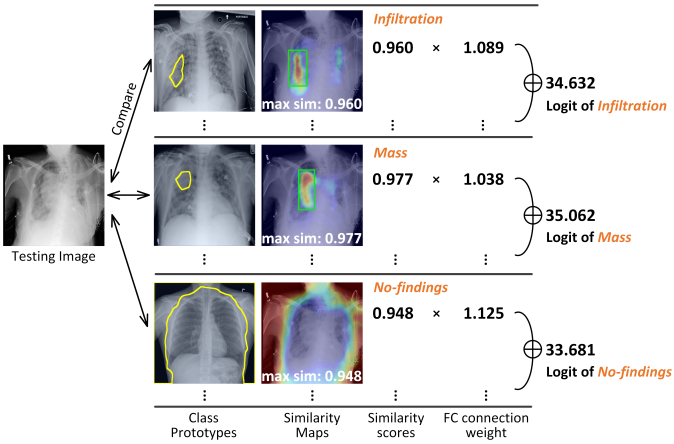

Fig. 5. A typical example of our CIPL method for multiple disease diagnosis interpretation from a testing chest X-ray image, where the green boxes indicate ground-truth disease annotations. For simplicity, the figure only illustrates one prototype and the corresponding similarity map from the class *infiltration*, *mass*, and *no-findings*.

annotations from radiologist's domain knowledge.

Table III gives the quantitative results of ophthalmic disease diagnosis on ODIR dataset. It is observed that our CIPL consistently produces the best average classification AUC results on both test sets. Importantly, CIPL substantially exceeds existing prototype-based methods [23], [24], [29], [69], by large margins of at least 2.9% and 3.1% (in mean AUC) on the on-site and off-site test sets, respectively, evidencing the effectiveness of cross- and intra-image prototypical learning for multi-label fundus image classification. We showcase typical visual prototypes of the *AMD* disease of different methods in Fig. 3(b). Our CIPL generates AMD prototypes that precisely cover the pathological lesions associated with the *AMD* disease, whereas the AMD prototypes from other compared methods are prone to be entangled with other diseases (see the white arrows), and in some cases, they completely neglect the actual *AMD* lesions (indicated by the white ellipses).

E. Weakly-supervised Multi-label Disease Localisation

We also evaluate the effectiveness of our CIPL method for localising thoracic diseases in a weakly-supervised setting on NIH ChestX-ray14, where the average class activation map is leveraged in the localisation process elaborated in Section IV-A. In this task, we compare with current SOTA weakly-supervised localisation approaches that are based on CAM [62], [64] and visual attentions [16], [75], [76]. Table IV presents the thresholded IoU accuracy results, where the types of explanation used for disease localisation are also provided. As can be seen, our CIPL demonstrates a significant enhancement in localisation accuracy across most diseases, at IoU thresholds of both 0.1 and 0.3, achieving the average accuracy of 0.78 and 0.47, respectively. Compared with previous leading saliency-based (e.g., CAM and visual attentions) localisation methods, our CIPL exhibits a much higher accuracy. In particular, CIPL also yields superior results over other prototype-based methods [24], [29], [69] that consider only individual-image information in prototype's learning. These improvements are attributed to the utilisation of rich cross-image semantics to accurately understand the pathological lesions of each disease class and beneficial intra-image cues to produce consistent and robust prototypes, evidenced by exhaustive ablation studies in the following Section IV-F.

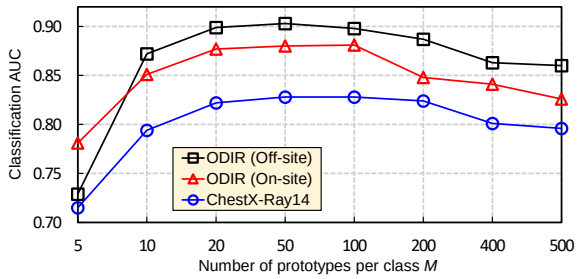

Fig. 6. Sensitivity of our CIPL method to the number of prototypes per class, measured by the average classification AUC performance.

F. Ablation Studies

1) Cross-image Prototypical Learning: We perform ablation experiments to study the effectiveness of our cross-image strategy in improving the disease classification and localisation performances. Table V provides the results on ODIR and ChestX-ray14, where the baseline CIPL only uses the basic training objective $\mathcal{L}_{basic}$, which is the same as the ProtoPNet [23] method. We notice that the cross-image prototypical learning strategy, denoted by $\mathcal{L}_{cross}$, can significantly improve the classification performance on both tasks. Also, this strategy greatly contributes to more accurate thoracic disease localisation, since it exploits common semantics of paired images to comprehensively understand the pathological lesions.

2) Intra-image Prototypical Learning: In Table V, we also provide ablation analysis for our intra-image prototypical learning strategy. Regarding the prediction alignment, one may have concerns about simply aligning predictions of the two views for each individual training sample, mentioned in Section III-C. Hence, we also provide such results by minimising the KL-divergence of predictions from two views of individual samples, denoted by $\mathcal{L}_{pred}{}^{\dagger}$. It can be noticed that, the interpretation alignment $\mathcal{L}_{inte}$ leads to significantly improved accuracy in the localisation of diseases since it is designed to make prototypes robust to two augmented image views. By contrast, the batch-level prediction alignment $\mathcal{L}_{pred}$ exhibits substantial gains in AUC classification performances, outperforming the sample-level prediction alignment $\mathcal{L}_{pred}{}^{\dagger}$, since $\mathcal{L}_{pred}$ considers holistic relationships among samples to provide more useful regularisation signals for the model.

3) Prototype Number: We study the sensitivity of our CIPL method to the number of prototypes per class M, as depicted in Fig. 6. As evident, the classification results generally exhibit robustness to M from 20 to 100. Nonetheless, a small number of prototypes leads to inadequate representation of rich and diverse patterns in training samples and results in sub-optimal results. Conversely, an excessive number of prototypes introduces unnecessary and even harmful information, causing a decline in performance and an escalation in model complexity. According to Fig. 6, we set the number of prototypes at 50 per class in all remaining experiments.

TABLE III
QUANTITATIVE RESULTS OF FUNDUS IMAGE CLASSIFICATION ON ODIR TEST SETS (ON-SITE AND OFF-SITE), REPORTED WITH THE AUC ON THE 7 DISEASES, MEAN AUC (MAUC), MEAN F1 (MF1), AND MEAN ACCURACY (MACC) METRICS. TOP-PART SHOWS GENERAL CLASSIFICATION METHODS AND BOTTOM PART SHOWS PROTOTYPE-BASED APPROACHES, WITH BEST RESULTS HIGHLIGHTED IN BOLD.

Method	On-site										Off-site									
	Diab	Glau	Cata	AMD	Hype	Myop	Othe	mAUC	mF1	mACC	Diab	Glau	Cata	AMD	Hype	Myop	Othe	mAUC	mF1	mACC
DB-Focal [32]	0.819	0.857	0.921	0.860	0.794	0.913	0.547	0.816±0.004	0.463±0.005	0.819±0.006	0.869	0.823	0.952	0.874	0.801	0.913	0.630	0.837±0.005	0.543±0.005	0.868±0.004
C-Tran [33]	0.853	**0.904**	0.949	0.863	0.802	0.941	0.628	0.848±0.003	0.498±0.004	0.901±0.004	0.895	0.834	0.969	0.903	0.819	0.949	0.693	0.866±0.004	0.592±0.004	0.886±0.003
CPCL [36]	0.871	0.896	0.967	0.870	0.803	0.929	0.651	0.855±0.003	0.503±0.003	0.895±0.003	0.907	0.839	0.972	**0.923**	0.809	0.955	0.706	0.873±0.003	0.605±0.003	0.909±0.002
TA-DCL [49]	0.877	0.873	0.971	**0.884**	0.793	0.935	0.677	0.858±0.002	0.508±0.003	0.894±0.003	0.915	0.855	0.977	0.916	0.789	0.956	0.720	0.875±0.002	0.607±0.003	0.917±0.003
ProtoPNet [23]	0.871	0.826	0.951	0.846	0.820	0.951	0.562	0.832±0.004	0.473±0.004	0.889±0.004	0.910	0.812	0.952	0.898	0.851	0.957	0.657	0.862±0.004	0.565±0.004	0.880±0.004
Deformable [24]	0.879	0.834	0.976	0.862	0.835	0.958	0.565	0.844±0.004	0.481±0.003	0.891±0.003	0.905	0.827	0.963	0.907	0.865	0.951	0.665	0.869±0.004	0.573±0.003	0.897±0.003
ProtoPNet++ [29]	0.881	0.801	**0.989**	0.849	0.844	0.941	0.631	0.848±0.003	0.496±0.004	0.894±0.004	0.913	0.815	0.976	0.901	0.860	0.943	0.683	0.870±0.004	0.601±0.004	0.904±0.003
PIP-Net [69]	0.882	0.850	0.941	0.852	0.843	0.942	0.650	0.851±0.003	0.498±0.003	0.896±0.002	0.903	0.828	0.953	0.900	**0.885**	0.935	0.701	0.872±0.003	0.592±0.003	0.911±0.002
CIPL	**0.896**	0.888	0.984	0.864	**0.867**	**0.963**	**0.696**	**0.880**±0.002	**0.553**±0.003	**0.911**±0.002	**0.930**	**0.869**	**0.990**	0.922	0.882	**0.993**	**0.738**	**0.903**±0.002	**0.620**±0.003	**0.934**±0.002

TABLE IV
WEAKLY-SUPERVISED THORACIC DISEASE LOCALISATION ACCURACY FROM DIFFERENT EXPLANATION METHODS: CLASS ACTIVATION MAP (CAM), ATTENTION MAP (ATTEN), AND PROTOTYPE (PROTO).

Method	T(IoU)	Type	Atel	Card	Effu	Infi	Mass	Nodu	Pnea	Pnex	Mean
Wang *et al.* [62]	0.1	CAM	0.69	0.94	0.66	0.71	0.40	0.14	0.63	0.38	0.57
Liu *et al.* [76]		Atten	0.39	0.90	0.65	0.85	0.69	0.38	0.30	0.39	0.60
Ouyang *et al.* [16]		Atten	**0.78**	0.97	**0.82**	0.85	0.78	0.56	0.76	0.48	0.75
ProtoPNet [23]		Proto	0.63	0.89	0.63	0.88	0.68	0.55	0.82	0.39	0.68
ProtoPNet++ [29]			0.67	0.90	0.65	0.92	0.74	0.58	0.90	0.39	0.72
Deformable [24]			0.70	0.92	0.65	**0.94**	0.71	**0.59**	0.92	0.45	0.74
CIPL			0.69	**1.00**	0.71	0.91	**0.85**	0.58	**0.98**	**0.48**	**0.78**
Wang *et al.* [62]	0.3	CAM	0.24	0.46	0.30	0.28	0.15	0.04	0.17	0.13	0.22
Cai *et al.* [75]		Atten	0.33	0.85	0.34	0.28	0.33	0.11	0.39	0.16	0.35
Ouyang *et al.* [16]		Atten	0.34	0.40	0.27	0.55	**0.51**	0.14	0.42	**0.22**	0.36
Liu *et al.* [76]		Atten	0.34	0.71	**0.39**	**0.65**	0.48	0.09	0.16	0.20	0.38
Hermoza *et al.* [64]		CAM	**0.37**	0.99	0.37	0.54	0.35	0.04	0.60	0.21	0.43
ProtoPNet [23]		Proto	0.29	0.83	0.21	0.42	0.37	0.19	0.50	0.14	0.37
ProtoPNet++ [29]			0.31	0.86	0.28	0.51	0.39	0.20	0.52	0.13	0.40
Deformable [24]			0.33	0.84	0.30	0.54	0.41	0.19	0.54	0.16	0.41
CIPL			0.33	**1.00**	0.26	0.53	0.47	**0.33**	**0.64**	0.18	**0.47**

TABLE V
ABLATION ANALYSIS OF OUR PROPOSED CIPL METHOD. WE GIVE AVERAGE CLASSIFICATION AUC RESULTS ON ODIR (ON-SITE) AND CHESTX-RAY14, AND AVERAGE THORACIC DISEASE LOCALISATION ACCURACY (LOC. ACC.) AT 0.3 IOU THRESHOLD.

$\mathcal{L}_{basic}$	$\mathcal{L}_{cross}$	$\mathcal{L}_{inte}$	$\mathcal{L}_{pred}{}^{\dagger}$	$\mathcal{L}_{pred}$	ODIR (AUC)	ChestX-ray14 AUC	ChestX-ray14 Loc. Acc.
✓					0.832	0.809	0.37
✓	✓				0.863	0.824	0.43
✓		✓			0.841	0.814	0.44
✓			✓		0.836	0.811	0.39
✓				✓	0.856	0.820	0.40
✓	✓	✓		✓	**0.880**	**0.828**	**0.47**

G. Single-label Diagnosis Scenario

Our CIPL method is developed to tackle the multi-label disease diagnosis and interpretation, but it is necessary to explore its effectiveness on the single-label diagnosis protocol. To achieve this, we adopt the chest X-ray dataset publicly accessible in [77]. The dataset comprises 5,856 paediatric chest X-ray images, with 5,232 samples for training and 624 samples for testing. These images are categorised into one of the following three classes: normal, bacterial pneumonia, and viral pneumonia. In this experiment, we employ the same training details (batch size, learning rate, per-class prototype number), hyper-parameters ($\alpha_1, \alpha_2, \alpha_3, \alpha_4$ and τ), and data augmentations, as elaborated in Section IV-B.

Table VI provides experimental results for the single-label chest X-ray classification task, where $\mathcal{L}_{intra} = \mathcal{L}_{inte} + \mathcal{L}_{pred}$, and we evaluate the overall sensitivity, specificity, precision, accuracy, and AUC score. As it can be observed, the cross-image training strategy $\mathcal{L}_{cross}$ enables slightly improved performances, compared with baseline CIPL only using $\mathcal{L}_{basic}$. This is due to only one type of disease in single-label training images, from which the learned prototypes are naturally disentangled. Combining with ablation results from Table V, it can be affirmed that our cross-image strategy is effective in tackling entangled multi-label disease diagnosis.

TABLE VI
CLASSIFICATION RESULTS OF OUR PROPOSED CIPL METHOD FROM SINGLE-LABEL PEDIATRIC CHEST X-RAY IMAGES.

Method	Sensitivity	Specificity	Precision	Accuracy	AUC
PIP-Net [69]	0.894	0.949	0.890	0.897	0.965
CIPL ($\mathcal{L}_{basic}$)	0.882	0.943	0.887	0.891	0.960
CIPL ($\mathcal{L}_{basic}$, $\mathcal{L}_{cross}$)	0.887	0.950	0.898	0.898	0.963
CIPL ($\mathcal{L}_{basic}$, $\mathcal{L}_{intra}$)	0.914	0.961	0.925	0.926	0.975
CIPL ($\mathcal{L}_{basic}$, $\mathcal{L}_{cross}$, $\mathcal{L}_{intra}$)	**0.918**	**0.964**	**0.930**	**0.931**	**0.976**

In Table VI, our proposed intra-image learning paradigm $\mathcal{L}_{intra}$ demonstrates notable performance improvements, since it leverages consistent and meaningful intra-image information in a self-supervised manner, regardless of whether the training images have single or multiple labels.

V. DISCUSSION

In this paper, we introduce the CIPL framework, designed to effectively learn disentangled prototypes for multi-label disease diagnosis. Our CIPL framework provides compelling similarity-based interpretations for the diagnosis decision with train-test associations, i.e, comparing testing samples with class-specific prototypes that represent particular regions of training images. In addition to relying on the region-level prototypes, the similarity-based interpretation can also be realised by image-level prototypes [78]–[80], which are produced through different learning techniques such as clustering [79] and auto-encoder models [78], [81]. However, these image-level prototypes are based on whole-image representations, resulting in less fine-grained interpretability compared to the region-level prototypes employed in our method. From a human user's perspective, understanding which parts of a testing image (e.g., pathological lesions in medical images) are similar to the region-level prototypes is more meaningful than merely determining whether the entire testing sample resembles the whole-image training prototypes.

Prototypical learning aims to find a set of class-specific prototypes to describe or summarise the training data, with inference relying on the similarities between testing samples

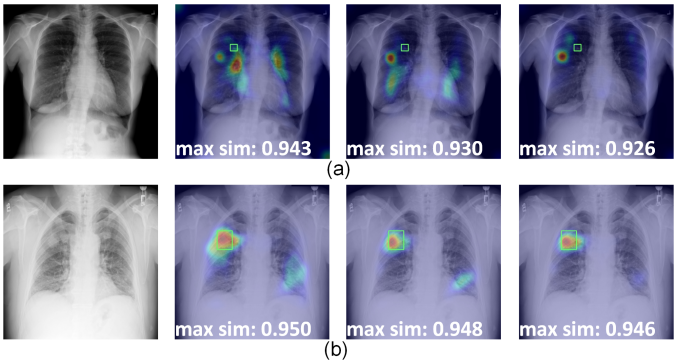

Fig. 7. Failure examples of our CIPL method. (a) mis-localisation of the subtle *nodule* lesion, where we show top-3 similarity maps with the true *nodule* class. (b) mis-classification for a *nodule* image, where we show top-3 similarity maps with the false predicted *mass* class. The green box in each similarity map denotes ground-truth *nodule* annotations.

and these prototypes. In this sense, the prototypical learning can be broadly categorised as a form of transductive reasoning [82], where distances or affinities to labelled reference samples are leveraged for the classification process. Even if the procedure is straightforward and well-understood by humans, its effectiveness often hinges on the complexity of the training data's distribution as well as the prototype's capacity of approximating such distribution [83]. This issue is clarified in Fig. 6, revealing that both an excessive or insufficient number of prototypes can negatively impact model performance.

While the prototype-based classification approach yields appealing interpretable results for disease diagnosis, our experiments still reveal some unfavourable failure cases that fall into two main types. 1) Mis-localisation of subtle pathological lesions, as shown in Fig. 7(a), occurs when the lesions (such as *nodule* highlighted by the green box) are extremely small, making them difficult to differentiate from the normal tissues and leading to the prototype activation in incorrect areas. It is noteworthy that the mis-localisation does not always cause wrong classification. Because of the model's transparency, such cases are easily identified, allowing for further model refinement. 2) Mis-classification to visually similar classes, as illustrated in Fig. 7(b), where the *mass* prototypes also activate the *nodule* lesion, resulting in a false positive prediction of the *mass* class. We believe that this is partly because both the *nodule* and *mass* have restricted and regular shape, which are poorly-distinguishable between them in the image. To address this, in the future we plan to incorporate constraints during training to encourage the prototype separability for these visually similar disease classes.

VI. Conclusion

In this work, we presented the CIPL method for multi-label disease diagnosis and interpretation from medical images. Our method leverages common cross-image semantics to disentangle the disease features of multiple classes, allowing for a more effective learning of class prototypes to comprehensively understand various pathological lesions. Moreover, our method exploits consistent intra-image information to enhance interpretation robustness and predictive performance, through an alignment-based regularisation strategy. Experimental results on two multi-label benchmarks illustrate the advantages of our CIPL over other competing approaches in disease classification and interpretation (measured by weakly-supervised localisation). Furthermore, our intra-image prototypical learning strategy is versatile and easily extended to tackle the single-label disease diagnosis and interpretation.

References

[1] Y. LeCun, Y. Bengio, and G. Hinton, "Deep learning," *Nature*, vol. 521, no. 7553, pp. 436–444, 2015.

[2] C. Wang, Y. Jin, X. Chen, and Z. Liu, "Automatic classification of volumetric optical coherence tomography images via recurrent neural network," *Sens. Imaging*, vol. 21, no. 1, p. 32, 2020.

[3] C. Ma, H. Wang, and S. C. Hoi, "Multi-label thoracic disease image classification with cross-attention networks," in *Proc. Int. Conf. Med. Image Comput. Comput.-Assist. Intervent.*, pp. 730–738, Springer, 2019.

[4] L. Fang, C. Wang, S. Li, H. Rabbani, X. Chen, and Z. Liu, "Attention to lesion: Lesion-aware convolutional neural network for retinal optical coherence tomography image classification," *IEEE Trans. Med. Imaging*, vol. 38, no. 8, pp. 1959–1970, 2019.

[5] Y. Chen, H. Wang, C. Wang, Y. Tian, F. Liu, Y. Liu, M. Elliott, D. J. McCarthy, H. Frazer, and G. Carneiro, "Multi-view local co-occurrence and global consistency learning improve mammogram classification generalisation," in *Proc. Int. Conf. Med. Image Comput. Comput.-Assist. Intervent.*, pp. 3–13, Springer, 2022.

[6] H. M. Frazer, C. A. Peña-Solorzano, C. F. Kwok, M. S. Elliott, Y. Chen, C. Wang, B. T. A.-Q. O. . F. S. K. . H. B. . K. R. . K. K. . L. S. . M. E. . . N. T. L. . R. P. B. . . S. D. . . W. P. C. 9, J. F. Lippey, J. L. Hopper, P. Brotchie, *et al.*, "Comparison of ai-integrated pathways with human-ai interaction in population mammographic screening for breast cancer," *Nat. Commun.*, vol. 15, no. 1, p. 7525, 2024.

[7] Y. Tian, G. Pang, F. Liu, Y. Liu, C. Wang, Y. Chen, J. Verjans, and G. Carneiro, "Contrastive transformer-based multiple instance learning for weakly supervised polyp frame detection," in *Proc. Int. Conf. Med. Image Comput. Comput.-Assist. Intervent.*, pp. 88–98, Springer, 2022.

[8] Y. Chen, Y. Liu, C. Wang, M. Elliott, C. F. Kwok, C. Peña-Solorzano, Y. Tian, F. Liu, H. Frazer, D. J. McCarthy, *et al.*, "Braixdet: Learning to detect malignant breast lesion with incomplete annotations," *Med. Image Anal.*, vol. 96, p. 103192, 2024.

[9] L. Fang, D. Cunefare, C. Wang, R. H. Guymer, S. Li, and S. Farsiu, "Automatic segmentation of nine retinal layer boundaries in oct images of non-exudative amd patients using deep learning and graph search," *Biomed. Opt. Express*, vol. 8, no. 5, pp. 2732–2744, 2017.

[10] C. Wang, Z. Cui, J. Yang, M. Han, G. Carneiro, and D. Shen, "Bowelnet: Joint semantic-geometric ensemble learning for bowel segmentation from both partially and fully labeled ct images," *IEEE Trans. Med. Imaging*, vol. 42, no. 4, pp. 1225–1236, 2023.

[11] Y. Liu, Y. Tian, C. Wang, Y. Chen, F. Liu, V. Belagiannis, and G. Carneiro, "Translation consistent semi-supervised segmentation for 3d medical images," *IEEE Trans. Med. Imaging*, 2024.

[12] C. Rudin, "Stop explaining black box machine learning models for high stakes decisions and use interpretable models instead," *Nat. Mach. Intell.*, vol. 1, no. 5, pp. 206–215, 2019.

[13] B. H. van der Velden, H. J. Kuijf, K. G. Gilhuijs, and M. A. Viergever, "Explainable artificial intelligence (xai) in deep learning-based medical image analysis," *Med. Image Anal.*, p. 102470, 2022.

[14] C. Patrício, J. C. Neves, and L. F. Teixeira, "Explainable deep learning methods in medical image classification: A survey," *ACM Comput. Surv.*, vol. 56, no. 4, pp. 1–41, 2023.

[15] R. R. Selvaraju, M. Cogswell, A. Das, R. Vedantam, D. Parikh, and D. Batra, "Grad-cam: Visual explanations from deep networks via gradient-based localization," in *Proc. IEEE Int. Conf. Comput. Vis.*, pp. 618–626, 2017.

[16] X. Ouyang, S. Karanam, Z. Wu, T. Chen, J. Huo, X. S. Zhou, Q. Wang, and J.-Z. Cheng, "Learning hierarchical attention for weakly-supervised chest x-ray abnormality localization and diagnosis," *IEEE Trans. Med. Imaging*, vol. 40, no. 10, pp. 2698–2710, 2020.

[17] S. Singla, M. Eslami, B. Pollack, S. Wallace, and K. Batmanghelich, "Explaining the black-box smoothly—a counterfactual approach," *Med. Image Anal.*, vol. 84, p. 102721, 2023.

[18] H. Shahamat and M. S. Abadeh, "Brain mri analysis using a deep learning based evolutionary approach," *Neural Netw.*, vol. 126, pp. 218–234, 2020.

[19] D. Mahapatra, A. Poellinger, and M. Reyes, "Interpretability-guided inductive bias for deep learning based medical image," *Med. Image Anal.*, vol. 81, p. 102551, 2022.

[20] L. Weber, S. Lapuschkin, A. Binder, and W. Samek, "Beyond explaining: Opportunities and challenges of xai-based model improvement," *Information Fusion*, vol. 92, pp. 154–176, 2023.

[21] J. Snell, K. Swersky, and R. Zemel, "Prototypical networks for few-shot learning," in *Proc. Adv. Neural Inf. Process. Syst.*, p. 30, 2017.

[22] T. Zhou, W. Wang, E. Konukoglu, and L. Van Gool, "Rethinking semantic segmentation: A prototype view," in *Proc. IEEE Conf. Comput. Vis. Pattern Recognit.*, pp. 2582–2593, 2022.

[23] C. Chen, O. Li, D. Tao, A. Barnett, C. Rudin, and J. K. Su, "This looks like that: deep learning for interpretable image recognition," in *Proc. Adv. Neural Inf. Process. Syst.*, pp. 795–807, 2019.

[24] J. Donnelly, A. J. Barnett, and C. Chen, "Deformable protopnet: An interpretable image classifier using deformable prototypes," in *Proc. IEEE Conf. Comput. Vis. Pattern Recognit.*, pp. 10265–10275, 2022.

[25] M. Sacha, D. Rymarczyk, Ł. Struski, J. Tabor, and B. Zieliński, "Protoseg: Interpretable semantic segmentation with prototypical parts," in *Proc. IEEE/CVF Winter Conf. Appl. Comput. Vis.*, pp. 1481–1492, 2023.

[26] H. Wu, C. Wang, L. Mei, T. Yang, M. Zhu, D. Shen, and Z. Cui, "Cephalometric landmark detection across ages with prototypical network," in *Proc. Int. Conf. Med. Image Comput. Comput.-Assist. Intervent.*, pp. 155–165, Springer, 2024.

[27] A. Aamodt and E. Plaza, "Case-based reasoning: Foundational issues, methodological variations, and system approaches," *AI communications*, vol. 7, no. 1, pp. 39–59, 1994.

[28] Y. Yang, Y. Zhuang, and Y. Pan, "Multiple knowledge representation for big data artificial intelligence: framework, applications, and case studies," *Front. Inf. Technol. Electron. Eng.*, vol. 22, no. 12, pp. 1551–1558, 2021.

[29] C. Wang, Y. Chen, Y. Liu, Y. Tian, F. Liu, D. McCarthy, M. Elliott, H. Frazer, and G. Carneiro, "Knowledge distillation to ensemble global and interpretable prototype-based mammogram classification models," in *Proc. Int. Conf. Med. Image Comput. Comput.-Assist. Intervent.*, pp. 1–9, Springer, 2022.

[30] L. S. Hesse and A. I. Namburete, "Insightr-net: Interpretable neural network for regression using similarity-based comparisons to prototypical examples," in *Proc. Int. Conf. Med. Image Comput. Comput.-Assist. Intervent.*, pp. 502–511, Springer, 2022.

[31] T. N. Wolf, S. Pölsterl, and C. Wachinger, "Don't panic: Prototypical additive neural network for interpretable classification of alzheimer's disease," in *International Conference on Information Processing in Medical Imaging*, pp. 82–94, Springer, 2023.

[32] T. Wu, Q. Huang, Z. Liu, Y. Wang, and D. Lin, "Distribution-balanced loss for multi-label classification in long-tailed datasets," in *European Conference on Computer Vision*, pp. 162–178, Springer, 2020.

[33] J. Lanchantin, T. Wang, V. Ordonez, and Y. Qi, "General multi-label image classification with transformers," in *Proc. IEEE Conf. Comput. Vis. Pattern Recognit.*, pp. 16478–16488, 2021.

[34] K. Yan, C. Zhang, J. Hou, P. Wang, Z. Bouraoui, S. Jameel, and S. Schockaert, "Inferring prototypes for multi-label few-shot image classification with word vector guided attention," in *Proc. AAAI Conf. Artif. Intell.*, vol. 36, pp. 2991–2999, 2022.

[35] J.-Y. Hang, M.-L. Zhang, Y. Feng, and X. Song, "End-to-end probabilistic label-specific feature learning for multi-label classification," in *Proc. AAAI Conf. Artif. Intell.*, vol. 36, pp. 6847–6855, 2022.

[36] F. Zhou, S. Huang, B. Liu, and D. Yang, "Multi-label image classification via category prototype compositional learning," *IEEE Trans. Circuits Syst. Video Technol.*, vol. 32, no. 7, pp. 4513–4525, 2021.

[37] P. Rajpurkar, J. Irvin, K. Zhu, B. Yang, H. Mehta, T. Duan, *et al.*, "Chexnet: Radiologist-level pneumonia detection on chest x-rays with deep learning," *arXiv preprint arXiv:1711.05225*, 2017.

[38] Y. Zhou, T. Zhou, T. Zhou, H. Fu, J. Liu, and L. Shao, "Contrast-attentive thoracic disease recognition with dual-weighting graph reasoning," *IEEE Trans. Med. Imaging*, vol. 40, no. 4, pp. 1196–1206, 2021.

[39] D. Mahapatra, A. J. Jimeno Yepes, S. Kuanar, S. Roy, B. Bozorgtabar, M. Reyes, and Z. Ge, "Class specific feature disentanglement and text embeddings for multi-label generalized zero shot cxr classification," in *Proc. Int. Conf. Med. Image Comput. Comput.-Assist. Intervent.*, pp. 276–286, Springer, 2023.

[40] U. Hasanah, C. Avian, J. T. Darmawan, N. Bachroin, M. Faisal, S. W. Prakosa, J.-S. Leu, and C.-T. Tsai, "Chexnet and feature pyramid network: a fusion deep learning architecture for multilabel chest x-ray clinical diagnoses classification," *Int. J. Card. Imaging*, vol. 40, no. 4, pp. 709–722, 2024.

[41] M. Faisal, J. T. Darmawan, N. Bachroin, C. Avian, J. S. Leu, and C.-T. Tsai, "Chexvit: Chexnet and vision transformer to multi-label chest x-ray image classification," in *IEEE International Symposium on Medical Measurements and Applications*, pp. 1–6, IEEE, 2023.

[42] F. Liu, Y. Chen, Y. Tian, Y. Liu, C. Wang, V. Belagiannis, and G. Carneiro, "Nvum: Non-volatile unbiased memory for robust medical image classification," in *Proc. Int. Conf. Med. Image Comput. Comput.-Assist. Intervent.*, pp. 544–553, Springer, 2022.

[43] Y. Chen, F. Liu, H. Wang, C. Wang, Y. Liu, Y. Tian, and G. Carneiro, "Bomd: bag of multi-label descriptors for noisy chest x-ray classification," in *Proc. IEEE/CVF Int. Conf. Comput. Vis.*, pp. 21284–21295, 2023.

[44] J. Xiao, Y. Bai, A. Yuille, and Z. Zhou, "Delving into masked autoencoders for multi-label thorax disease classification," in *Proc. IEEE/CVF Winter Conf. Appl. Comput. Vis.*, pp. 3588–3600, 2023.

[45] K. He, X. Chen, S. Xie, Y. Li, P. Dollár, and R. Girshick, "Masked autoencoders are scalable vision learners," in *Proc. IEEE/CVF Conf. Comput. Vis. Pattern Recognit.*, pp. 16000–16009, 2022.

[46] N. N. Agu, J. T. Wu, H. Chao, I. Lourentzou, A. Sharma, M. Moradi, P. Yan, and J. Hendler, "Anaxnet: anatomy aware multi-label finding classification in chest x-ray," in *Proc. Int. Conf. Med. Image Comput. Comput.-Assist. Intervent.*, pp. 804–813, Springer, 2021.

[47] W. Nie, C. Zhang, D. Song, L. Zhao, Y. Bai, K. Xie, and A. Liu, "Deep reinforcement learning framework for thoracic diseases classification via prior knowledge guidance," *Comput. Med. Imaging Graph.*, vol. 108, p. 102277, 2023.

[48] M. I. Hossain, M. Zunaed, M. K. Ahmed, S. J. Hossain, A. Hasan, and T. Hasan, "Thorax-priornet: A novel attention-based architecture using anatomical prior probability maps for thoracic disease classification," *IEEE Access*, 2023.

[49] Y. Zhang, L. Luo, Q. Dou, and P.-A. Heng, "Triplet attention and dual-pool contrastive learning for clinic-driven multi-label medical image classification," *Med. Image Anal.*, vol. 86, p. 102772, 2023.

[50] Y. Zhang, H. Jiang, Y. Miura, C. D. Manning, and C. P. Langlotz, "Contrastive learning of medical visual representations from paired images and text," in *Machine Learning for Healthcare Conference*, pp. 2–25, PMLR, 2022.

[51] C. Wu, X. Zhang, Y. Zhang, Y. Wang, and W. Xie, "Medklip: Medical knowledge enhanced language-image pre-training for x-ray diagnosis," in *Proc. IEEE/CVF Int. Conf. Comput. Vis.*, pp. 21372–21383, 2023.

[52] X. Zhang, C. Wu, Y. Zhang, W. Xie, and Y. Wang, "Knowledge-enhanced visual-language pre-training on chest radiology images," *Nat. Commun.*, vol. 14, no. 1, p. 4542, 2023.

[53] T. Dai, R. Zhang, F. Hong, J. Yao, Y. Zhang, and Y. Wang, "Unichest: Conquer-and-divide pre-training for multi-source chest x-ray classification," *IEEE Trans. Med. Imaging*, 2024.

[54] C. Wang, Y. Liu, Y. Chen, F. Liu, Y. Tian, D. McCarthy, H. Frazer, and G. Carneiro, "Learning support and trivial prototypes for interpretable image classification," in *Proc. IEEE/CVF Int. Conf. Comput. Vis.*, pp. 2062–2072, 2023.

[55] C. Wang, Y. Chen, F. Liu, M. Elliott, C. F. Kwok, C. Pena-Solorzano, H. Frazer, D. J. McCarthy, and G. Carneiro, "An interpretable and accurate deep-learning diagnosis framework modelled with fully and semi-supervised reciprocal learning," *IEEE Trans. Med. Imaging*, 2023.

[56] X. Lu, W. Wang, C. Ma, J. Shen, L. Shao, and F. Porikli, "See more, know more: Unsupervised video object segmentation with co-attention siamese networks," in *Proc. IEEE/CVF Conf. Comput. Vis. Pattern Recognit.*, pp. 3623–3632, 2019.

[57] X. Lu, W. Wang, J. Shen, D. J. Crandall, and L. Van Gool, "Segmenting objects from relational visual data," *IEEE Trans. Pattern Anal. Mach. Intell.*, vol. 44, no. 11, pp. 7885–7897, 2021.

[58] X. Li, T. Zhou, J. Li, Y. Zhou, and Z. Zhang, "Group-wise semantic mining for weakly supervised semantic segmentation," in *Proc. AAAI Conf. Artif. Intell.*, vol. 35, pp. 1984–1992, 2021.

[59] H. Wang, W. Wang, T. Shu, W. Liang, and J. Shen, "Active visual information gathering for vision-language navigation," in *European Conference on Computer Vision*, pp. 307–322, Springer, 2020.

[60] L. Jing and Y. Tian, "Self-supervised visual feature learning with deep neural networks: A survey," *IEEE Trans. Pattern Anal. Mach. Intell.*, vol. 43, no. 11, pp. 4037–4058, 2020.

[61] K. He, H. Fan, Y. Wu, S. Xie, and R. Girshick, "Momentum contrast for unsupervised visual representation learning," in *Proc. IEEE Conf. Comput. Vis. Pattern Recognit.*, pp. 9729–9738, 2020.

[62] X. Wang, Y. Peng, L. Lu, Z. Lu, M. Bagheri, and R. M. Summers, "Chestx-ray8: Hospital-scale chest x-ray database and benchmarks on weakly-supervised classification and localization of common thorax

diseases," in *Proc. IEEE Conf. Comput. Vis. Pattern Recognit.*, pp. 2097–2106, 2017.

[63] N. Li, T. Li, C. Hu, K. Wang, and H. Kang, "A benchmark of ocular disease intelligent recognition: One shot for multi-disease detection," in *Benchmarking, Measuring, and Optimizing: Third BenchCouncil International Symposium*, pp. 177–193, Springer, 2021.

[64] R. Hermoza, G. Maicas, J. C. Nascimento, and G. Carneiro, "Region proposals for saliency map refinement for weakly-supervised disease localisation and classification," in *Proc. Int. Conf. Med. Image Comput. Comput.-Assist. Intervent.*, pp. 539–549, Springer, 2020.

[65] Y. Xie, Q. Wan, H. Xie, Y. Xu, T. Wang, S. Wang, and B. Lei, "Fundus image-label pairs synthesis and retinopathy screening via gans with class-imbalanced semi-supervised learning," *IEEE Trans. Med. Imaging*, 2023.

[66] S. Guendel, S. Grbic, B. Georgescu, S. Liu, A. Maier, and D. Comaniciu, "Learning to recognize abnormalities in chest x-rays with location-aware dense networks," in *Iberoamerican Congress on Pattern Recognition*, pp. 757–765, Springer, 2019.

[67] B. Qi, G. Zhao, X. Wei, C. Du, C. Pan, Y. Yu, and J. Li, "Gren: graph-regularized embedding network for weakly-supervised disease localization in x-ray images," *IEEE J. Biomed. Health Inform.*, vol. 26, no. 10, pp. 5142–5153, 2022.

[68] Q. Guan and Y. Huang, "Multi-label chest x-ray image classification via category-wise residual attention learning," *Pattern Recognit. Lett.*, vol. 130, pp. 259–266, 2020.

[69] M. Nauta, J. Schlötterer, M. van Keulen, and C. Seifert, "Pip-net: Patch-based intuitive prototypes for interpretable image classification," in *Proc. IEEE/CVF Conf. Comput. Vis. Pattern Recognit.*, pp. 2744–2753, 2023.

[70] E. Kim, S. Kim, M. Seo, and S. Yoon, "Xprotonet: diagnosis in chest radiography with global and local explanations," in *Proc. IEEE Conf. Comput. Vis. Pattern Recognit.*, pp. 15719–15728, 2021.

[71] G. Huang, Z. Liu, L. Van Der Maaten, and K. Q. Weinberger, "Densely connected convolutional networks," in *Proc. IEEE Conf. Comput. Vis. Pattern Recognit.*, pp. 4700–4708, 2017.

[72] K. He, X. Zhang, S. Ren, and J. Sun, "Deep residual learning for image recognition," in *Proc. IEEE Conf. Comput. Vis. Pattern Recognit.*, pp. 770–778, 2016.

[73] F. Isensee, T. Wald, C. Ulrich, M. Baumgartner, S. Roy, K. Maier-Hein, and P. F. Jaeger, "nnu-net revisited: A call for rigorous validation in 3d medical image segmentation," *arXiv preprint arXiv:2404.09556*, 2024.

[74] A. E. Johnson, T. J. Pollard, N. R. Greenbaum, M. P. Lungren, C.-y. Deng, Y. Peng, Z. Lu, R. G. Mark, S. J. Berkowitz, and S. Horng, "Mimic-cxr-jpg, a large publicly available database of labeled chest radiographs," *arXiv preprint arXiv:1901.07042*, 2019.

[75] J. Cai, L. Lu, A. P. Harrison, X. Shi, P. Chen, and L. Yang, "Iterative attention mining for weakly supervised thoracic disease pattern localization in chest x-rays," in *Proc. Int. Conf. Med. Image Comput. Comput.-Assist. Intervent.*, pp. 589–598, Springer, 2018.

[76] J. Liu, G. Zhao, Y. Fei, M. Zhang, Y. Wang, and Y. Yu, "Align, attend and locate: Chest x-ray diagnosis via contrast induced attention network with limited supervision," in *Proc. IEEE Int. Conf. Comput. Vis.*, pp. 10632–10641, 2019.

[77] D. S. Kermany, M. Goldbaum, W. Cai, C. C. Valentim, H. Liang, S. L. Baxter, A. McKeown, G. Yang, X. Wu, F. Yan, *et al.*, "Identifying medical diagnoses and treatable diseases by image-based deep learning," *Cell*, vol. 172, no. 5, pp. 1122–1131, 2018.

[78] O. Li, H. Liu, C. Chen, and C. Rudin, "Deep learning for case-based reasoning through prototypes: A neural network that explains its predictions," in *Proc. AAAI Conf. Artif. Intell.*, vol. 32, 2018.

[79] W. Wang, C. Han, T. Zhou, and D. Liu, "Visual recognition with deep nearest centroids," in *International Conference on Learning Representations*, pp. 1–15, 2023.

[80] L. S. Hesse, N. K. Dinsdale, and A. I. Namburete, "Prototype learning for explainable brain age prediction," in *Proc. IEEE/CVF Winter Conf. Appl. Comput. Vis.*, pp. 7903–7913, 2024.

[81] S. Gautam, A. Boubekki, S. Hansen, S. Salahuddin, R. Jenssen, M. Höhne, and M. Kampffmeyer, "Protovae: A trustworthy self-explainable prototypical variational model," in *Proc. Adv. Neural Inf. Process. Syst.*, vol. 35, pp. 17940–17952, 2022.

[82] Y. Mao, N. Wang, W. Zhou, and H. Li, "Joint inductive and transductive learning for video object segmentation," in *Proc. IEEE/CVF Int. Conf. Comput. Vis.*, pp. 9670–9679, 2021.

[83] C. Wang, Y. Chen, F. Liu, Y. Liu, D. J. McCarthy, H. Frazer, and G. Carneiro, "Mixture of gaussian-distributed prototypes with generative modelling for interpretable and trustworthy image recognition," *arXiv preprint arXiv:2312.00092*, 2023.